

Organic Solar Cells with 20.12% Efficiency Enabled by Monosubstituted Carbazole-Based Self-Assembled Monolayers

Qiaonan Chen,[#] Jingnan Wu,[#] Maureen Gumbo, Leandro R. Franco, Kangbo Sun, Lunjie Zeng, Xianjie Liu, Yufei Wang, Donghong Yu, Lars Öhrström, Mailde S. Ozório, Alexandre Holmes, C. Moyses Araujo, Eva Olsson, Mats Fahlman, Renqiang Yang,^{*} and Ergang Wang^{*}



Cite This: *ACS Energy Lett.* 2025, 10, 5584–5595



Read Online

ACCESS |

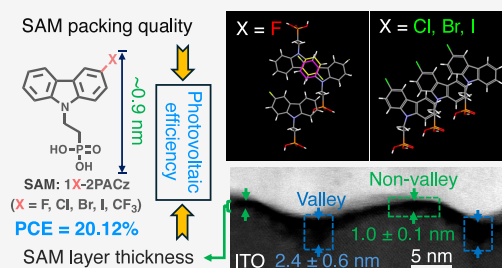
 Metrics & More

 Article Recommendations

 Supporting Information

ABSTRACT: Carbazole-derived self-assembled monolayer (SAM) materials as hole transport layers are widely used in organic photovoltaics, yet the role of subtle substituent effects on interfacial structure and device performance remains underexplored. Here, we systematically investigate monosubstituted carbazole SAMs (1X-2PACz, X = F, Cl, Br, I, CF₃) on indium tin oxide (ITO) and their device performance. Fluorine substitution achieves the highest surface coverage but poor interfacial order, while bulky 1CF₃-2PACz introduces interfacial disorder. In contrast, Cl-, Br-, and I-substituted SAMs exhibit favorable packing and work-function alignment, enabling efficiencies of up to 19.03% in PM6:L8-BO and 20.12% in D18:L8-BO based solar cells.

Crucially, cross-sectional scanning transmission electron microscopy provides the first direct visualization of the nonideal SAM morphologies on ITO, revealing molecular aggregates in ITO valleys, mono- or multilayers on flat regions, and incomplete surface coverage. These findings establish how substituents and processing critically govern interfacial packing and photovoltaic efficiency, guiding SAM-based interfacial design.



The hole transport layer (HTL),^{1–6} together with its counterpart—the electron transport layer (ETL),^{7–10} plays a crucial role in enhancing power conversion efficiencies (PCEs) to 18–20% for organic solar cells (OSCs), on top of the adoption of innovative light-harvesting polymer donors^{11–14} and nonfullerene acceptors nowadays.^{15–22} Notably, replacing traditional PEDOT:PSS HTL that are acidic and corrosive to the indium–tin-oxide (ITO) electrodes, with novel self-assembled monolayer (SAM) materials has further improved PCE by 1–2% and enhanced device stability, highlighting SAMs' potential for further optimization on both stability and photovoltaic (PV) performance.^{1,2,4–6,23,24} It should be noted that the so-called SAM materials in OSCs do not form ideal self-assembled monolayers; however, due to its widespread adoption in the field, the term “SAM” is still used in this work.

Recent studies on SAM molecules in OSCs have mainly focused on modifying functional conjugated headgroups. Common strategies include altering the conjugated backbone structure, molecular size and symmetry,^{2,4,25–27} or introducing substituents (e.g., F, Cl, Br, I, methyl, methoxy, and glycol) onto the carbazole headgroup (Figure 1A).^{5,24,28–33} These modifications modulate the molecular dipole, tuning the work function (WF) of the modified ITO electrode and influencing

energy level alignment with the active layer.^{2,4,23,29,34,35} They also impact SAM intermolecular interactions and ITO surface coverage, thereby influencing hole extraction and active layer morphology, ultimately affecting PCE of OSCs.^{3,30,31} These studies revealed that a relatively higher WF and shorter alkyl linkers contribute to enhanced PCEs. Moreover, monosubstituted SAMs, such as 1Cl- and 1Br-2PACz, achieved impressive PCEs of 19.0% and 19.35%, respectively. Notably, 1Br-2PACz outperformed its disubstituted counterpart 2Br-2PACz (18.32%) (Figure 1B),^{29,31} which highlights the potential of monosubstituted SAMs over disubstituted SAMs in OSC performance optimization. Compared with the relatively high WF of disubstituted SAMs, the monosubstituted systems could effectively reduce the WF, resulting in better alignment with the active layer. However, systematic studies on various monosubstituted groups (e.g., F, Cl, Br, I, and CF₃)

Received: August 13, 2025

Revised: October 6, 2025

Accepted: October 13, 2025

Previous work

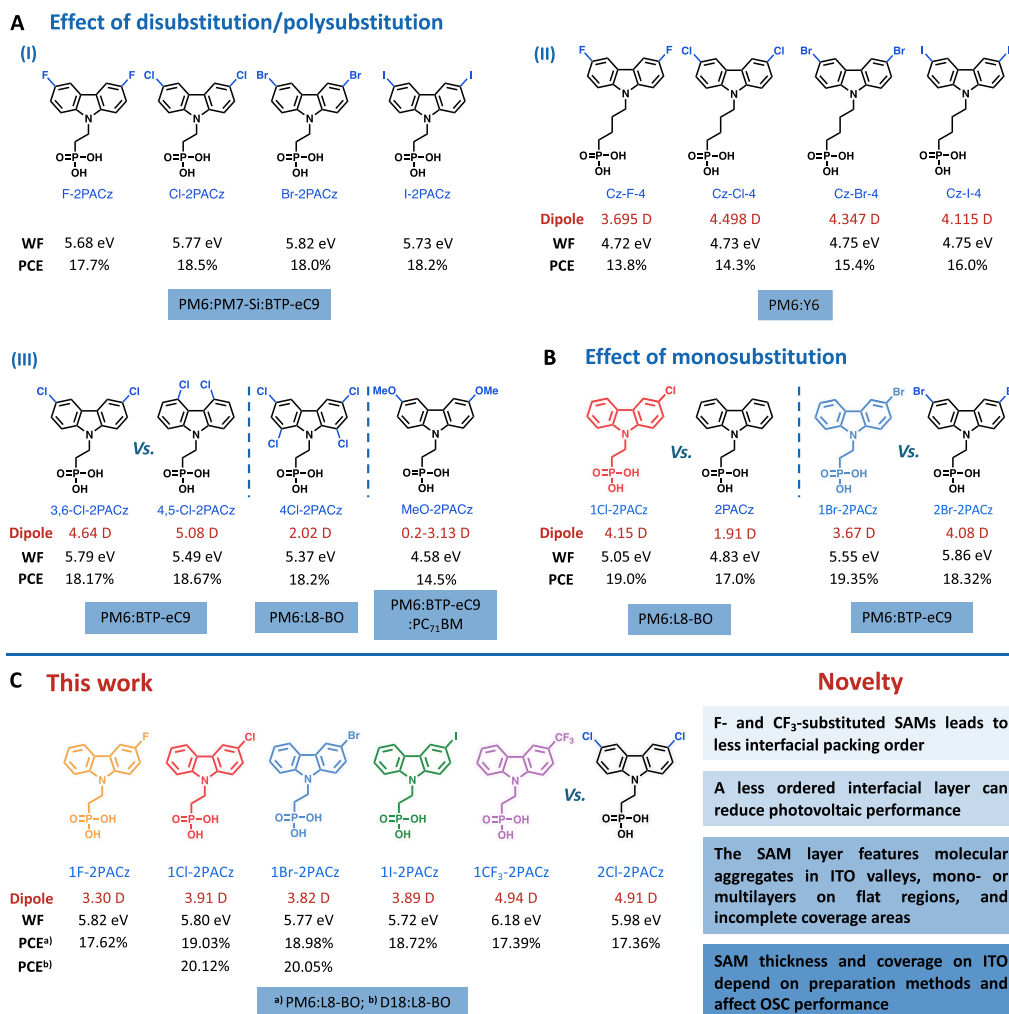


Figure 1. Previously reported studies on the substitution effects of SAMs, including (A) disubstitution/polysubstitution and (B) monosubstitution, and their impact on molecular dipole moment, WF, and PCE of OSCs. (C) The structures, molecular dipole moment, and WF of SAMs, PCE of OSCs, and the novelty of this work.

remained limited, particularly regarding their effects on intermolecular interactions, WF, surface coverage, and interfacial packing order on modified ITO, as well as the overall OSC performance.

Moreover, research on the effects of different post-treatment methods for spin-coated SAM layers (no rinsing, rinsing with SAM solution, and rinsing with methanol) on SAM thickness and coverage on ITO remains insufficiently explored, which is crucial for understanding the correlation between SAM layer packing quality and OSC performance.^{3,36–39} To date, only a few perovskite solar cells have employed cross-sectional scanning transmission electron microscopy (STEM) to compare SAM layer thickness and coverage.^{38,40} However, the cross-sectional STEM images in these studies show limited resolution, making it difficult to analyze ultrathin SAM layers, particularly their packing quality on the ITO, such as surface coverage and layer thickness. These are key issues in SAM research and highlight the need for further investigation.^{41–46}

To address these key challenges, we designed a series of monosubstituted carbazole-based SAMs (1X-2PACz, where X = F, Cl, Br, I, or CF₃) (Figure 1C). Devices incorporating 1Cl-, 1Br-, and 1I-2PACz achieved higher PCEs, up to 20.12%,

attributed to improved interfacial packing and better energy level alignment. In contrast, 1F-2PACz exhibited highest ITO surface coverage but suffered from antiparallel π - π stacking of carbazole units, while the bulky CF₃ group in 1CF₃-2PACz induced steric hindrance and interfacial disorder, both leading to lower efficiencies. Aberration-corrected cross-sectional STEM reveals how SAM packing and surface coverage on the ITO vary with different rinsing treatments, directly influencing the photovoltaic performance of the OSCs. These results provide critical insights into the correlation between SAM structure, HTL interfacial properties, and OSC performance, addressing key knowledge gaps in current SAM research.

Figure 2A illustrates the chemical structures of five monosubstituted SAM molecules (1F-, 1Cl-, 1Br-, 1I-, and 1CF₃-2PACz), synthesized via a three-step procedure (Scheme S1, detailed in the Supporting Information). SAM layers were formed by spin-coating a 0.3 mg/mL ethanol solution onto ITO, followed by thermal annealing at 85 °C for 5 min and two rinses with the same solution.^{4,5,25} The dipole moments of aryl headgroup³⁰ and WFs of SAM molecules adsorb on the (111) termination of ITO were calculated by density

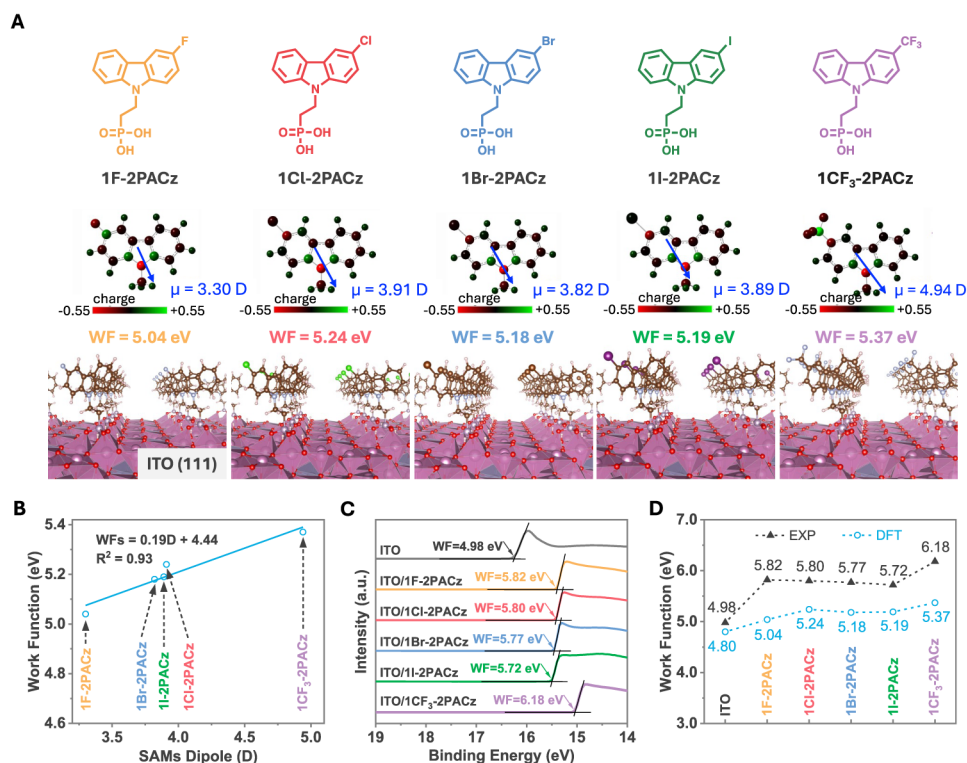


Figure 2. (A) Molecular structures, simulated dipole moments, and simulated WFs of ITO modified with various hole-selective materials: 1F-, 1Cl-, 1Br-, 1I-, and 1CF₃-2PACz. (B) Dipole-dependency on simulated WF for SAMs. (C) UPS spectra (using the He I lamp with a photon energy of 21.22 eV) of bare and SAMs-modified ITO. (D) Comparison of WF from UPS and DFT results.

functional theory (DFT) with B3LYP/31G (d, p) basis set (Figure 2A).^{3,5} 1Cl-, 1Br-, and 1I-2PACz showed similar dipole moments (\sim 3.82–3.91 D), while 1F-2PACz was lower (3.30 D) due to fluorine's weak conjugation and small size. In contrast, 1CF₃-2PACz had a much higher dipole moment (4.94 D) from the strong electron-withdrawing CF₃ group. A larger vertical dipole could enhance the ITO WF,^{3,47} improving energy level alignment with the donor HOMO and facilitating hole extraction.^{2,4,29} The simulated WFs for 1F-, 1Cl-, 1Br-, 1I-, and 1CF₃-2PACz modified ITO were 5.04, 5.24, 5.18, 5.19, and 5.37 eV, respectively (Figure S1), showing an approximately linear relationship with dipole moment (Figure 2B).

Ultraviolet photoelectron spectrometry (UPS) was used to evaluate monosubstitution effects on the ITO WF. The bare ITO exhibited slightly higher WF of 4.98 eV (\sim 0.28 eV²⁹ above typical values of \sim 4.70 eV,^{4,8,21} due to fluorine incorporation as shown in Figure S2A). After calibration, the SAM-modified ITOs showed further WF elevation: 1F-, 1Cl-, 1Br-, 1I-, and 1CF₃-2PACz yielded WFs of 5.54, 5.52, 5.49, 5.44, and 5.90 eV, respectively (Figure 3C). Halogen substituents led to the resulting WF within \sim 0.1 eV difference from the PM6 HOMO (-5.50 eV),⁴⁸ enabling nearly barrier-free hole transport. In contrast, the strongly electron-withdrawing CF₃ group significantly raised the WF, creating an energy offset relative to that of the PM6 HOMO and leading to a Schottky-type contact that hinders hole extraction. It is noteworthy that the WF trends of all SAM molecules measured by UPS matched the DFT simulations except for 1F-2PACz (Figure 2D). This deviation may stem from higher surface coverage or different molecular orientation, as both can

increase WF,^{3,49,50} which is further supported by surface coverage analysis below.

To verify the coverage differences of SAMs on ITO, X-ray photoelectron spectroscopy (XPS) was conducted (Figure S2).³¹ Relative coverage factors calculated from the peak areas of C 1s and In 3d_{2/3} in high-resolution XPS spectra (Figure S3) were 1.51×10^{-2} , 0.99×10^{-2} , 1.06×10^{-2} , 0.95×10^{-2} , and 1.04×10^{-2} for 1F-, 1Cl-, 1Br-, 1I-, and 1CF₃-2PACz, respectively (Figure 3A and Table S1). Notably, 1F-2PACz exhibited a significantly higher surface coverage than all the other SAMs, likely correlated with the smaller fluorine size and denser intermolecular packing.

Furthermore, the absorption spectra of the SAM molecules in ethanol were measured via UV-vis spectroscopy (Figure 3B and Table S2). The short maximum absorption wavelength and low absorption coefficient help minimize parasitic absorption of sunlight, allowing the active layer to harvest more photons and thereby enhance the short-circuit current (J_{sc}). The experimental absorption results align well with the trend simulated by DFT calculations, as detailed in Figures S4 and S5 and Table S3.

To investigate the effect of processing methods on SAM surface coverage, three common preparation methods were evaluated on SAM surface coverage, as shown in Figure 3D: (i) direct spin-coating of SAM solutions onto ITO substrates (0.3 mg mL^{-1} , $150 \mu\text{L}$, 3000 rpm), followed by thermal annealing at 85°C for 5 min;^{29,31,37,50,51} (ii) the same process followed by two rinses with SAM solution ($150 \mu\text{L}$, 6000 rpm);^{4,5,25,34} (iii) the same process followed by two rinses with methanol ($150 \mu\text{L}$, 6000 rpm).^{1,3,24,33,52}

UV-vis absorption spectra for different quartz/SAM layers prepared via these methods were compared (Figure 3E).

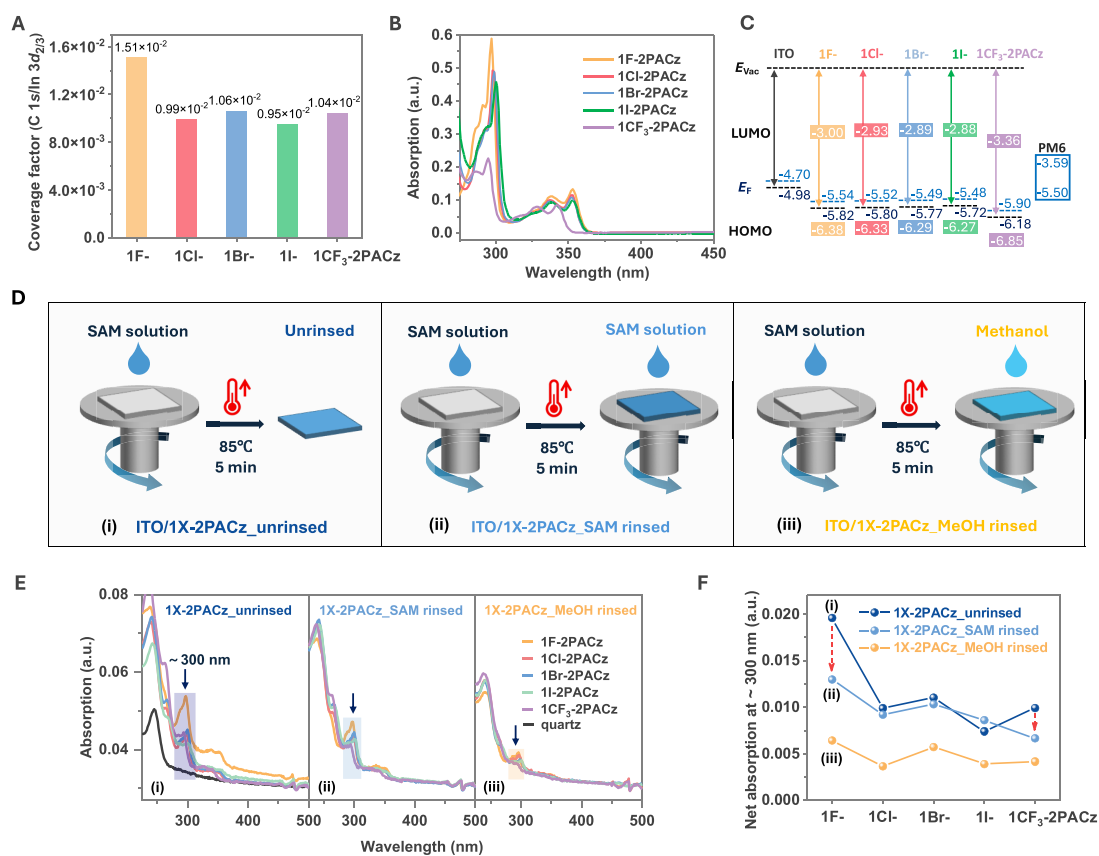


Figure 3. (A) The relative coverage factor of SAMs-modified ITO (with SAM solution-rinsed). (B) UV-vis absorption spectra of SAM molecules in their ethanol solutions (3×10^{-5} M). (C) UPS-measured energy levels of fluorine-containing ITO (4.98 eV)/SAMs (marked in black) and the corresponding calibrated ITO (4.70 eV)/SAMs (marked in blue), together with the HOMO and LUMO levels of PM6. (D) SAM-modified ITO under three different processing conditions: (i) unrinsed, (ii) with SAM solution-rinsed, and (iii) with methanol-rinsed. (E) UV-vis absorption spectra of SAM-modified quartz under different processing conditions. (F) Comparison of the net absorption intensity variation at ~ 300 nm.

Quartz was used instead of ITO glass to decrease the absorption of the substrate in the UV region. The typical absorption peak at ~ 300 nm, was selected for comparison (Figure 3F). Specifically, 1Cl-, 1Br-, and 1I-2PACz SAM layers maintained similar absorption intensity following SAM solution rinsing, indicating the formation of more ordered and stable molecular assemblies on ITO. Conversely, layers of 1F- and 1CF₃-2PACz showed notable intensity decrease after SAM solution rinsing, suggesting a less ordered SAM packing and a lower degree of ITO/quartz-binded molecules, making their removal easier during post-treatment. These results indicate that 1F- and 1CF₃-substituted SAMs exhibit lower stability and less-ordered packing compared to 1Cl-, 1Br-, and 1I-substituted analogs. Moreover, methanol rinsing notably reduced absorption intensity (~ 300 nm) of all SAMs' films, suggesting the removal of loosely bound SAM molecules, likely resulting in a monolayer structure.³⁸ However, UV-vis spectroscopy alone is insufficient for accurately determining the thickness and coverage of the SAM layer; therefore, cross-sectional STEM was employed to directly visualize and validate these parameters.

As illustrated in Figure 4A–C,^{38,40} aberration-corrected cross-sectional high-angle annular dark-field STEM (HAADF-STEM) was employed to investigate differences in SAM layers prepared using the three different SAMs treatment shown in Figure 3D. The device structure used here was ITO/SAM (1F-2PACz)/Au/(Pd/C), with Au and Pd/C layers replacing the

active layer to enhance image contrast.³⁸ The lattice structures of Au and ITO are visible in the images, showing the atomic scale resolution of HAADF-STEM.

Due to atomic number differences, the SAM layer appears as a darker region between the ITO and Au layers. Cross-sectional HAADF-STEM images show that the ITO surface is uneven, with valley-like features between elongated grains (blue arrows/dashed box), consistent with scanning electron microscope (SEM) images showing grain major axes of 10–50 nm and minor axes of 5–20 nm (Figure S6).³⁸ These valleys lead to local SAM molecule accumulation, increasing hole tunneling distances. Measured valley depths were 2.1 ± 0.5 (unrinsed), 2.4 ± 0.6 (SAM-rinsed), and 1.8 ± 0.6 nm (MeOH-rinsed). Notably, methanol rinsing reduces molecules accumulation in valley region by removing loosely bound molecules, consistent with reduced absorbance near ~ 300 nm (Figure 3F).

In flat regions (green arrows/dashed box), the SAM thickness remained uniform at 0.8 ± 0.1 , 1.0 ± 0.1 , and 0.8 ± 0.2 nm for (i) ITO/1F-2PACz_unrinsed, (ii) ITO/1F-2PACz_SAM rinsed, and (iii) ITO/1F-2PACz_MeOH rinsed, respectively. Given the molecular height of ~ 0.9 nm (Figure S7), the slightly larger thickness of 1.0 ± 0.1 nm observed in the SAM-rinsed sample likely indicates the presence of an ordered edge-on monolayer overlaid by one or more loosely packed face-on layers. In contrast, methanol rinsing removes these upper layers, leaving the film close to a monolayer ($0.8 \pm$

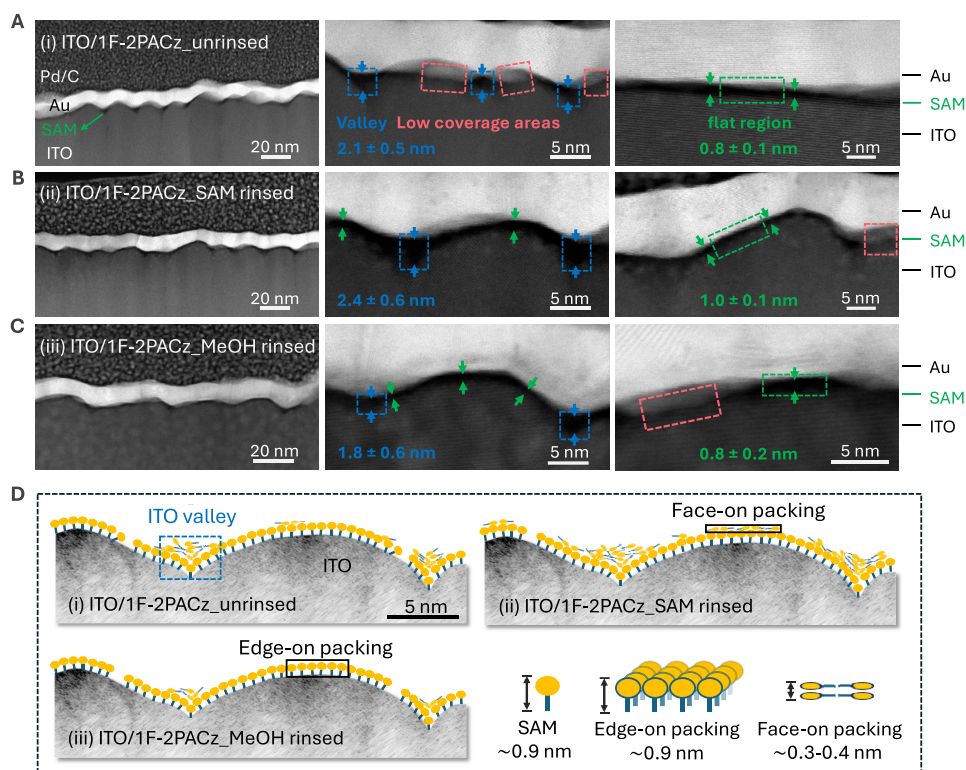


Figure 4. Investigation of thickness and coverage of the ITO/1F-2PACz layer processed from different methods. SAMs sandwiched between ITO and Au layer. Cross-sectional HAADF-STEM images of (A) ITO/1F-2PACz_unrinsed, (B) ITO/1F-2PACz_SAM rinsed, and (C) ITO/1F-2PACz_MeOH rinsed. (D) Schematic illustration of SAM layers on ITO processed using different methods. The packing distance in edge-on and face-on orientations were inferred based on single crystal analysis.

0.2 nm) in the flat regions.^{38,53,54} Notably, SAM solution rinsing yields a more continuous and uniform film in the flat regions with fewer surface defects. To verify that this behavior is not specific to 1F-2PACz, we further investigated the chloro-substituted 1Cl-2PACz (Figure S8). In this case, methanol-rinsed SAMs exhibited extended flat regions with near-monolayer or even depleted coverage, in clear contrast to the higher coverage films obtained via SAM solution rinsing. Similar to 1F-2PACz, methanol rinsing reduces surface coverage, whereas SAM solution rinsing preserves a more continuous film, underscoring that this trend is common across different monosubstituted SAMs.

Figure 4D illustrates the ITO/SAM morphology under different treatments. (i) Without rinsing, limited coverage and valley molecule accumulation occur, with flat regions forming near-monolayers. (ii) SAM solution rinsing enhances film continuity but leads to more valley molecule accumulation and multilayers with mixed orientations (edge-on at the bottom and face-on on top) in flat regions, slightly increasing hole tunneling distance. (iii) Methanol rinsing reduces both surface coverage and valley molecule accumulation, forming a monolayer in flat regions. As both excessive accumulation and insufficient coverage hinder hole transport, thinner and more uniform SAM layers are preferred for optimal performance. These morphological differences provide a reasonable explanation for the resulting PCE variations and reproducibility issues in OSCs.^{41,55,56} Devices using SAM solution-rinsed (PCE = 17.62%) and MeOH-rinsed (PCE = 17.77%) films outperformed unrinsed ones (PCE = 14.86%) (Figure S9 and Table S4). SAM solution-rinsing, however, appeared as a more reliable technique to avoid the formation of depleted areas. To

simplify the comparison, we used the SAM solution-rinsing method for all of the other measurements in this work.

The surface morphology of ITO/SAM substrates, reflecting interfacial layer packing quality, was investigated by using tapping-mode atomic force microscopy (AFM). As shown in Figure S10, 1CF₃-2PACz exhibited the lowest surface roughness, with the root-mean-squared (RMS) roughness of 1.75 nm. In contrast, other halogenated SAMs showed similar roughness values (~3 nm), suggesting more consistent packing. This indicates that 1CF₃-2PACz exhibits a markedly different packing behavior compared with the other halogenated SAMs. The bulky CF₃ group may disrupt ordered packing, promoting molecular accumulation in ITO valleys and resulting in an overall smoother surface. Contact-angle measurements (Figure S11) and calculated surface energies (Tables S5 and S6) showed minimal variation among halogenated SAMs (~44–48 mJ/m²), while 1CF₃-2PACz exhibited a significantly lower surface energy (28.78 mJ/m²). This suggests poorer wettability and compatibility with the active layer, likely leading to a less favorable morphology and reduced device performance.

The thermal stability of various SAM molecules was evaluated by thermogravimetric analysis (TGA), indicating that their 5% weight loss temperatures of 1F-, 1Cl-, 1Br-, 1I-, and 1CF₃-2PACz are 315, 305, 254, 210, and 156 °C, respectively (Figure S12 and Table S7). The gradual decrease correlates with increasing halogen size and the electron-withdrawing nature of these functional groups, likely weakening the bond between the carbazole core and substituents. Despite this variation, all SAMs maintain sufficient thermal stability for their optoelectronic applications.

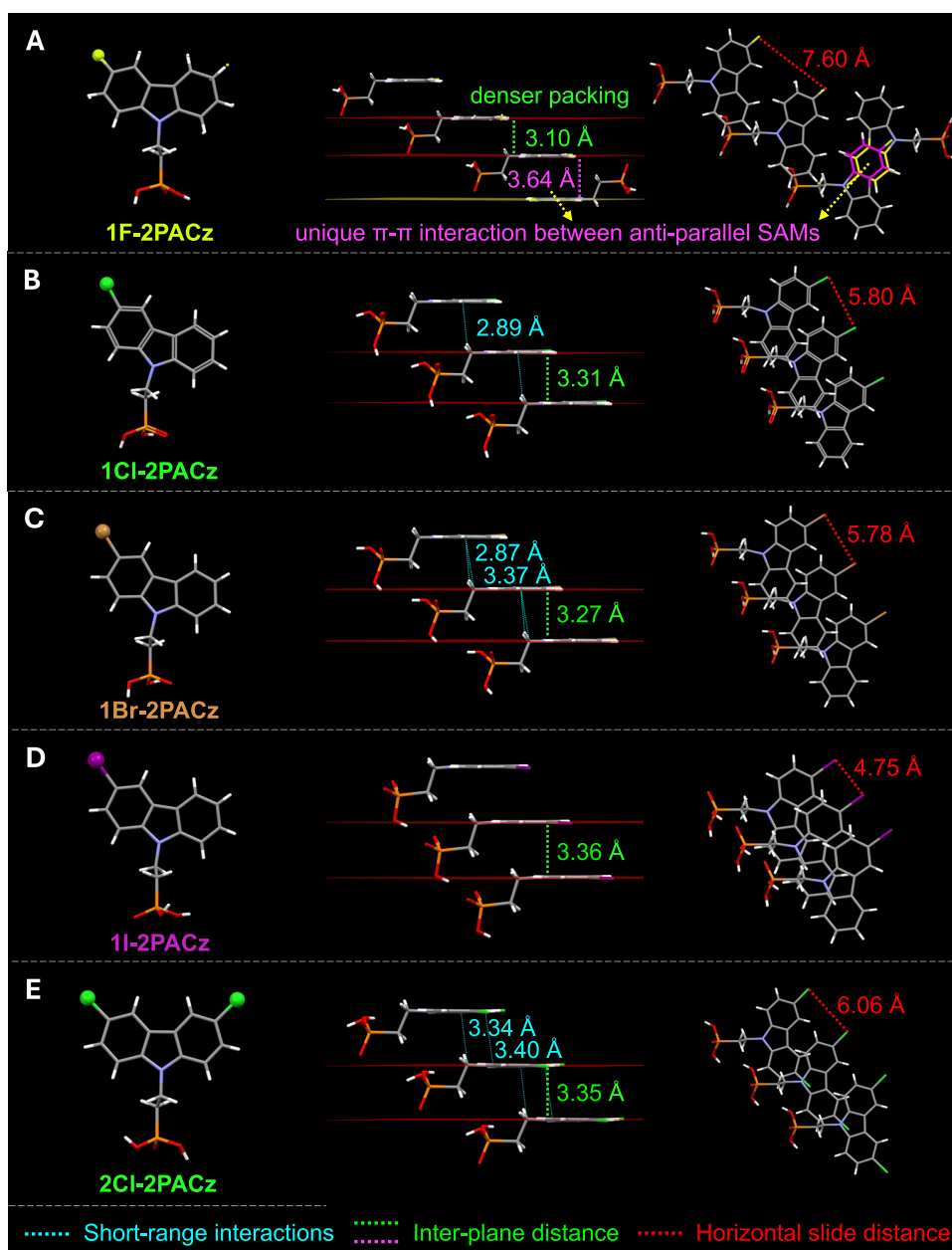


Figure 5. Molecular packing patterns of SAMs observed in single crystals: (A) 1F-2PACz, (B) 1Cl-2PACz, (C) 1Br-2PACz, (D) 1I-2PACz, and (E) 2Cl-2PACz (1Cl-2PACz (2303762) and 2Cl-2PACz (2352347) are retrieved from the CCDC database; 1F-2PACz (2440287), 1Br-2PACz (2440288), and 1I-2PACz (2440285) are obtained in this work).

Furthermore, differential scanning calorimetry (DSC) thermograms (Figure S13) reveal that most SAMs have clear melting points above 200 °C, indicating ordered crystalline packing. In contrast, 1CF₃-2PACz shows only two low-temperature transitions (45.0 and 85.2 °C), suggesting internal structural rearrangements rather than melting, consistent with its smoother but less ordered morphology on ITO. Overall, these results reveal how the bulky -CF₃ decrease crystallinity and reduce both thermal and structural stability of 1CF₃-2PACz.

To better understand the self-assembly behavior of SAMs on ITO, we analyzed the single-crystal structures of 2PACz derivatives (1F-, 1Cl-, 1Br-, 1I-, 2Cl-) and their corresponding carbazole cores (Figures 5, S14, and S15; Table S8). Single crystal of 1CF₃-2PACz is difficult to obtain, likely due to steric hindrance from the bulky CF₃ group. Among the SAMs, 1F-

2PACz showed the shortest interplane stacking distance (3.10 Å), compared to 1Cl- (3.31 Å), 1Br- (3.27 Å), 1I- (3.36 Å), and 2Cl-2PACz (3.35 Å), suggesting denser packing due to the smallest atomic size of fluorine. This correlates with its higher surface coverage on the ITO (Figure 3A). Additionally, 1F-2PACz exhibited a unique antiparallel π - π stacking (3.64 Å), absent in other SAMs, which may introduce interfacial disorder on ITO, potentially affect hole extraction and overall interfacial packing quality. This may explain the sharp drop in the 300 nm absorption after SAM rinsing (Figure 3E), as loosely bound 1F-2PACz molecules are likely washed away.

Furthermore, the single-crystal structures of pristine carbazole headgroups (1F-, 1Cl-, 1Br-, 1I-, and 2Cl-carbazole) were compared to assess the intrinsic interactions among different halogen-substituted anchoring groups. As shown in Figure S14, 1F- and 2Cl-carbazoles exhibited tighter packing

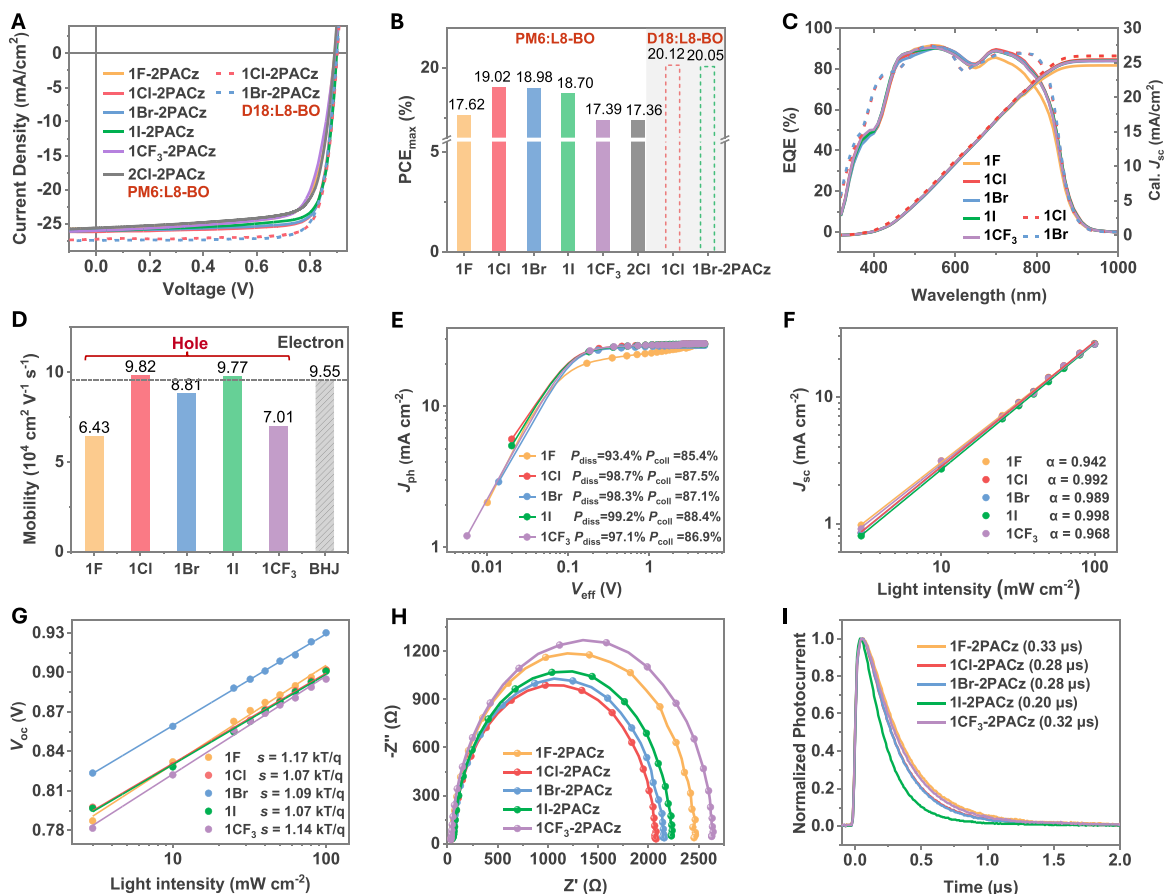


Figure 6. (A) J - V characteristics, (B) comparison of PCE, and (C) EQE spectra of optimal PM6:L8-BO and D18:L8-BO OSCs with different HTLs. (D) Hole- and electron-mobilities of the devices. (E) Characteristics of J_{ph} vs V_{eff} . Light intensity dependence on (F) J_{sc} and (G) V_{oc} for the optimized PSCs. (H) EIS of OSCs with different hole-selective contacts. (I) Normalized TPC graphs of OSC devices with different HTLs.

Table 1. Photovoltaic Parameters of OSCs Based on PM6:L8-BO and D18:L8-BO BHJs with Different SAM HTLs Measured under Illumination with AM 1.5G (100 mW cm^{-2})

HTLs	V_{oc} [V]	J_{sc} [mA cm^{-2}]	J_{cal}^a [mA cm^{-2}]	FF [%]	PCE ^b [%]	R_s [Ω]	R_{int} [Ω]
1F-2PACz ^c	0.894	25.72	24.59	76.6	17.62 (16.90 \pm 0.24)	96.2	2401
1Cl-2PACz ^c	0.900	26.21	25.43	80.7	19.03 (18.66 \pm 0.17)	62.7	1998
1Br-2PACz ^c	0.898	25.98	25.22	81.4	18.98 (18.77 \pm 0.10)	62.5	2073
1I-2PACz ^c	0.895	26.02	25.29	80.4	18.72 (18.58 \pm 0.08)	57.5	2159
1CF ₃ -2PACz ^c	0.895	26.04	25.26	74.4	17.39 (16.97 \pm 0.21)	86.8	2574
2Cl-2PACz ^c	0.893	25.63		75.9	17.36	64.1	
1Cl-2PACz ^d	0.903	27.29	25.93	81.7	20.12 (19.92 \pm 0.14)	49.0	
1Br-2PACz ^d	0.901	27.45	25.97	81.1	20.05 (19.44 \pm 0.50)	51.9	

^aThe integral J_{sc} values were calculated from the EQE curves. ^bThe average PCE values in brackets were obtained from 11 independent devices.

^cThe active layer is PM6:L8-BO. ^dThe active layer is D18:L8-BO.

with smaller interplane distances (2.55 Å and 2.54 Å) and more short-range interactions than 1Cl-, 1Br-, and 1I-carbazoles (2.65–2.68 Å). This indicates that fluorine substitution enhances packing density and disubstitution (2Cl) yields slightly denser packing than 1Cl-, consistent with XPS results showing higher ITO surface coverage for 2Cl-2PACz.

The photovoltaic performance of monosubstituted SAMs and 2Cl-2PACz as HTLs was evaluated in OSCs with the device structure: ITO/SAMs/PM6:L8-BO/PDINN/Ag. As shown in Figure 6A and Table 1, devices using 1Cl-, 1Br-, and 1I-2PACz showed superior PCEs (19.03%, 18.98%, and

18.72%) and high FFs (80.7%, 81.4%, and 80.4%), along with J_{sc} values above 25.9 mA cm^{-2} . In contrast, devices with 1F-, 1CF₃-, and 2Cl-2PACz delivered lower PCEs (\sim 17.4–17.6%) and FFs (74.4–76.6%) (Figure 6B). The J_{sc} values for 1F- and 2Cl-2PACz were slightly lower (\sim 25.63–25.72 mA cm^{-2}). The calculated photocurrent density (J_{cal}) from the external quantum efficiency (EQE) measurements closely matched J_{sc} to within 4% (Figure 6C). Moreover, the active layer was replaced with D18:L8-BO, resulting in further improved PCEs of 20.12% and 20.05% for devices using 1Cl- and 1Br-2PACz HTLs, respectively (Figure 6A). The enhancements were primarily attributed to a significant increase in J_{sc} (Table 1).

Using PM6:L8-BO as a representative system, the observed differences in PCE among the SAMs are mainly due to variations in FF, which correlate with the series resistance (R_s), as summarized in Table 1. R_s was extracted by fitting the J - V curves measured under illumination. SAMs with Cl-, Br-, and I-substituents exhibited lower R_s values than those with F- and CF₃-, indicating that the SAM layer significantly influences charge transport and interfacial contact between the electrode and the active layer. The higher R_s and reduced FF of 1F- and 1CF₃-2PACz are likely due to their less ordered interfacial structures. Notably, although 2Cl-2PACz exhibits stronger molecular packing and higher surface coverage than 1Cl-2PACz, the latter yields better performance. This is likely related to its slightly lower WF of 1Cl-2PACz, which aligns more favorably with HOMO of PM6 (-5.50 eV).^{4,8,16,21}

Hole (μ_h) and electron (μ_e) mobilities of the OSCs were evaluated via the space charge limited current (SCLC) method on the optimized devices with the architecture of ITO/SAMs/active layer (100 nm)/MoO₃ (10 nm)/Ag (Figure 6D and Figure S16). The μ_h of 1F-/1Cl-/1Br-/1I-/1CF₃-2PACz-based devices are $6.43 \times 10^{-4}/9.82 \times 10^{-4}/8.81 \times 10^{-4}/9.77 \times 10^{-4}/7.01 \times 10^{-4}$ cm² V⁻¹ s⁻¹, respectively, while μ_e was 9.55×10^{-4} cm² V⁻¹ s⁻¹. Notably, 1Cl-, 1Br-, and 1I-2PACz exhibit a higher μ_h and a more balanced ratio of μ_h/μ_e than 1F- and 1CF₃-2PACz. While the trend in μ_h appears to align with FF and PCE, it should be emphasized that the SCLC model assumes ohmic contacts. Since SAM layers can influence injection barriers, the observed differences in extracted μ_h may arise from variations in interfacial charge injection rather than from intrinsic hole transport in the bulk active layer. Therefore, the SAMs primarily affect interfacial transport properties, which in turn contribute to the observed differences in FF and device performance.

Exciton dissociation probabilities (P_{diss} , under J_{sc} conditions) and charge collection efficiencies (P_{coll} at the maximum power point) were calculated as 93.4/85.4, 98.7/87.5, 98.3/87.1, 99.2/88.4, and 97.1%/86.9% for devices based on 1F-, 1Cl-, 1Br-, 1I-, and 1CF₃-2PACz, respectively (Figure 6E). The higher P_{diss} and P_{coll} values for 1Cl-, 1Br-, and 1I-2PACz-based devices indicate superior exciton dissociation and enhanced charge collection, contributing to their higher J_{sc} and FF. Conversely, 1F- and 1CF₃-2PACz, with the lower P_{diss} and P_{coll} values, exhibit reduced J_{sc} and FF. In addition, the dependencies of J_{sc} (Figure 6F) and V_{oc} (Figure 6G) on light intensity (P_{light}), were analyzed to further study the charge recombination mechanism. The relationship between J_{sc} and P_{light} can be defined as $J_{\text{sc}} \propto (P_{\text{light}})^{\alpha}$, where an α value close to 1 suggests weak bimolecular recombination. The α values of 1Cl-2PACz (0.992), 1Br-2PACz (0.989), and 1I-2PACz (0.998) are evidently higher than that of 1F-2PACz (0.942) and 1CF₃-2PACz (0.968), suggesting more bimolecular recombination in the latter devices. Additionally, the relationship between P_{light} and V_{oc} follows $V_{\text{oc}} \propto nkT/q \ln P$ (k , T , and q are the Boltzmann constant, the temperature in Kelvin, and elementary charge, respectively), where an n value close to 1 indicates a weak trap-assisted charge recombination. OSCs based on 1Cl-2PACz (1.07 kT/q), 1Br-2PACz (1.09 kT/q), and 1I-2PACz (1.07 kT/q) show smaller slopes than those of 1F-2PACz (1.17 kT/q) and 1CF₃-2PACz (1.14 kT/q), again revealing stronger trap-assisted or geminate recombination for the latter two devices. The above results all point toward the idea that SAMs substitution influences the charge-dissociation, -collection, and -recombination of their OSCs, ultimately

affecting the FF and PCE. This could be attributed to the inferior interfacial layer quality of 1F-2PACz- and 1CF₃-2PACz-modified ITO.

Furthermore, electrochemical impedance spectroscopy (EIS) was conducted for carrier mobilities and lifetime.^{32,57,58}

Figure 6H presents the Nyquist plots of various OSC cells, with fitting results detailed in Figure S17 and Table S9. Remarkably, the device resistance includes electrode resistance (R_{ele}), interface resistance (R_{int}), and bulk heterojunction (BHJ) layer resistances (R_{bhj}). Devices based on 1F- and 1CF₃-2PACz exhibited relatively high device resistance of 2454.2 and 2629.6 Ω , respectively. Whereas 1Cl-, 1Br-, and 1I-2PACz displayed lower and more comparable device resistances of 2075.7, 2157.2, and 2228.9 Ω , respectively. Notably, R_{int} values for 1F-, 1Cl-, 1Br-, 1I-, and 1CF₃-2PACz, are 2401, 1998, 2073, 2159, and 2574 Ω , respectively, playing utmost role in device resistance, closely aligning with their PV performances, particularly the FF. This demonstrates that the SAM layer packing quality has a substantial impact on R_{int} , thereby significantly influencing charge transport and extraction.

To obtain further insight into the carrier decay dynamics in these devices, transient photocurrent (TPC) experiments were carried out.⁵⁹ As shown in Figure 6I, ITO/1I-2PACz has the shortest charge carrier extraction time of 0.20 μs , while 1Cl- and 1Br-2PACz exhibit a slightly longer time of 0.28 μs each. In contrast, 1F- and 1CF₃-2PACz have the longest extraction time of 0.33 and 0.32 μs , respectively. This is roughly consistent with the PV performance, indicating enhanced charge extraction process in 1Cl-, 1Br-, and 1I-2PACz-based devices when anchored to ITO substrates. These results confirm that the improved interfacial packing quality of Cl-, Br-, and I-substituted SAMs effectively reduce both series resistance and interfacial resistance, facilitates charge extraction, and thereby contributes to the enhanced FF and PCE. To assess how HTLs influence active layer morphology and molecular packing, PM6:L8-BO films spin-coated on five SAM-modified substrates were analyzed via AFM and two-dimensional grazing incidence wide-angle X-ray scattering (2D GIWAXS). AFM images (Figure S18) show similar surface roughness (RMS 1.95–2.21 nm) and well-ordered nanofibrils for films on 1F-, 1Cl-, 1Br-, and 1I-2PACz, indicating smooth, uniform morphologies. While, the active layer based on 1CF₃-2PACz exhibits a smoother surface (RMS 1.28 nm), consistent with the lower surface energy and the flatter surface of the 1CF₃-2PACz film. GIWAXS measurements (Figure S19, Tables S10 and Table S11) reveal that all films exhibit similar face-on orientations and nearly identical diffraction peak positions and crystal coherence lengths (CCL), except for 1F-2PACz, which shows a slightly longer in-plane CCL (54.11 \AA). Overall, the active layers exhibit comparable crystallinity across different HTLs.

These results suggest that the active layers on all HTLs possess similar crystallinity with no significant differences observed across the five films. However, only the BHJ film on 1CF₃-2PACz displays a markedly distinct surface morphology. This implies that for HTLs based on 1F-, 1Cl-, 1Br-, and 1I-2PACz, PV performance is primarily governed by the intrinsic quality of the HTL itself. In contrast, the lower PV performance observed for 1CF₃-2PACz may be attributed to a combination of its inferior HTL properties, higher WF, and unfavorable active layer morphology.

Based on the above discussions, the substituent groups on SAMs play a crucial role in modulating the WF, surface

coverage, interfacial packing order, and ultimately the photovoltaic performance of OSCs, particularly FF and PCE. Halogen-substituted SAMs with tuned WFs of 5.44–5.54 eV exhibit favorable alignment with the HOMO level of PM6 (−5.50 eV), thereby facilitating efficient hole extraction. In contrast, the excessively deep WF of 1CF₃-2PACz hinders charge transfer across the interface, resulting in a reduced photovoltaic efficiency. Although 1F-2PACz showed the highest surface coverage on ITO substrates, single-crystal structural analysis revealed distinctive head-to-head, antiparallel π – π interactions between carbazole moieties. These interactions introduce interfacial packing disorder, which undermines the benefits of high coverage. Similarly, for 1CF₃-2PACz, the bulky CF₃ substituents disrupt regular molecular packing, resulting in a disordered HTL morphology. Therefore, the relatively lower PV performance observed in devices incorporating 1F- and 1CF₃-2PACz SAMs as HTLs can be attributed to nonoptimal HTL quality. Additionally, the notably high WF of 1CF₃-2PACz further impeded efficient hole transport and extraction, negatively impacting the overall device performance.

In summary, we have systematically investigated the effects of monosubstituted carbazole-based SAMs (1X-2PACz, where X = F, Cl, Br, I, or CF₃) on the interfacial properties and photovoltaic performance of OSCs. Our findings reveal that Cl, Br, I-substituted SAMs significantly improve device performance, achieving PCEs of up to 20.12%, by enhancing interfacial molecular packing, promoting balanced charge transport, and reducing series/interfacial resistance. In contrast, 1F- and 1CF₃-2PACz suffer from less ordered packing and inferior charge extraction, leading to diminished FF and PCE. Notably, cross-sectional STEM imaging provides the first direct visualization of the nonideal morphology of SAMs on ITO surfaces, showing the presence of molecular aggregates in ITO valleys, mono- or multilayers on flat regions, and partial surface coverage in some areas. The SAM thickness and coverage were found to strongly depend on processing conditions, correlating closely with the photovoltaic performance. Overall, this work underscores the crucial role of substitution groups and processing strategies in modulating the interfacial properties of SAMs, providing important insights for molecular design and interfacial engineering toward high-performance OSCs.

■ ASSOCIATED CONTENT

SI Supporting Information

The Supporting Information is available free of charge at <https://pubs.acs.org/doi/10.1021/acsenergylett.5c02585>.

Details of synthetic procedures, material characterizations, solar cell fabrication and characterization, XPS, contact angle measurements, GIWAXS fitting, single-crystal X-ray diffraction (CCDC 2440287, 2440288, 2440285, and 2440286), theoretical modeling, and AFM analysis (PDF)

■ AUTHOR INFORMATION

Corresponding Authors

Renqiang Yang – Key Laboratory of Optoelectronic Chemical Materials and Devices (Ministry of Education) School of Optoelectronic Materials and Technology, Jiangnan University, Wuhan 430056, China; Email: yangrq@jhun.edu.cn

Ergang Wang – Department of Chemistry and Chemical Engineering, Chalmers University of Technology, Göteborg SE-412 96, Sweden; School of Materials Science and Engineering, Zhengzhou University, Zhengzhou 450001, China; orcid.org/0000-0002-4942-3771; Email: ergang@chalmers.se

Authors

Qiaonan Chen – Department of Chemistry and Chemical Engineering, Chalmers University of Technology, Göteborg SE-412 96, Sweden

Jingnan Wu – Department of Chemistry and Chemical Engineering, Chalmers University of Technology, Göteborg SE-412 96, Sweden

Maureen Gumbo – Department of Chemistry and Chemical Engineering, Chalmers University of Technology, Göteborg SE-412 96, Sweden

Leandro R. Franco – Department of Chemistry and Chemical Engineering, Chalmers University of Technology, Göteborg SE-412 96, Sweden; Department of Engineering and Physics, Karlstad University, Karlstad 65188, Sweden

Kangbo Sun – College of New Materials and New Energies, Shenzhen Technology University, Shenzhen 518118, China

Lunjie Zeng – Department of Physics, Chalmers University of Technology, Göteborg SE-412 96, Sweden; orcid.org/0000-0002-4564-7217

Xianjie Liu – Laboratory of Organic Electronics (LOE), Department of Science and Technology, Linköping University, 60174 Norrköping, Sweden; orcid.org/0000-0002-3190-2774

Yufei Wang – College of New Materials and New Energies, Shenzhen Technology University, Shenzhen 518118, China

Donghong Yu – Department of Chemistry and Bioscience, Aalborg University, Aalborg DK-9220, Denmark; Sino-Danish Center for Education and Research, Aarhus DK-8000, Denmark; School of Materials Science and Engineering, Zhengzhou University, Zhengzhou 450001, China; orcid.org/0000-0002-3035-5035

Lars Öhrström – Department of Chemistry and Chemical Engineering, Chalmers University of Technology, Göteborg SE-412 96, Sweden; orcid.org/0000-0002-6420-2141

Maike S. Ozório – Department of Chemistry, University of Copenhagen, Copenhagen DK-2100, Denmark

Alexandre Holmes – Department of Chemistry and Chemical Engineering, Chalmers University of Technology, Göteborg SE-412 96, Sweden; orcid.org/0009-0003-1340-4602

C. Moyses Araujo – Department of Engineering and Physics, Karlstad University, Karlstad 65188, Sweden; Materials Theory Division, Department of Physics and Astronomy, Uppsala University, Uppsala 75120, Sweden; orcid.org/0000-0001-5192-0016

Eva Olsson – Department of Physics, Chalmers University of Technology, Göteborg SE-412 96, Sweden; orcid.org/0000-0002-3791-9569

Mats Fahlman – Laboratory of Organic Electronics (LOE), Department of Science and Technology, Linköping University, 60174 Norrköping, Sweden; orcid.org/0000-0001-9879-3915

Complete contact information is available at: <https://pubs.acs.org/10.1021/acsenergylett.5c02585>

Author Contributions

[#]These authors contributed equally to this work (Q.C. and J.W.).

Notes

The authors declare no competing financial interest.

ACKNOWLEDGMENTS

We thank the Swedish Research Council (2019-04683, 2020-05223), the Swedish Research Council Formas (2023-01008, 2024-01110), the Wallenberg Foundation (2022.0192), the Wallenberg Initiative Materials Science for Sustainability (WISE-AP01-D19), the Guangdong Basic and Applied Basic Research Foundation (2022A1515010875), the Shenzhen Key Laboratory of Applied Technologies of Super-Diamond and Functional Crystals (ZDSYS20230626091303007) for financial support. Support from Sino-Danish Center is gratefully acknowledged. R.Y. thanks the National Natural Science Foundation of China (22375077, 52573276, 52073122) for financial support. M.G. and L.Ö. thank the Chalmers Area of Advance Nano for financial support. M. S. O. acknowledges the Pioneer Center for Accelerating P2X Materials Discovery (CAPEX), DNRf grant number P3, and the Danish National Research Foundation, Center for High Entropy Alloy Catalysis (CHEAC) DNRf149. We thank Chalmers Materials Analysis Laboratory, CMAL, and the Olle Engqvist Foundation. Computations were performed at NSC Tetralith provided by the National Academic Infrastructure for Supercomputing in Sweden (NAISS) funded by the Swedish Research Council through grant agreement no. 2022-06725 (NAISS). Swedish Research Council and Swedish Foundation for Strategic Research are acknowledged for access to ARTEMI, the Swedish National Infrastructure in Advanced Electron Microscopy (2021-00171 and RIF21-0026).

REFERENCES

- (1) Zhang, N.; Jiang, W.; An, Y.; Liu, Q.; Du, G.; Xia, T.; Chen, D.; Wong, C. T.; Zeng, X. C.; Lin, F. R.; Jen, A. K. Y.; Yip, H. L. Enhancing UV Stability and Charge Extraction in Organic Solar Cells with Phenyl-Linked Aromatic Self-Assembled Monolayer. *Adv. Funct. Mater.* **2025**, *35*, 2423178.
- (2) Liu, L.; Yu, F.; Hu, D.; Jiang, X.; Huang, P.; Li, Y.; Tian, G.; Lei, H.; Wu, S.; Tu, K.; Chen, C.; Gu, T.; Chen, Y.; Duan, T.; Xiao, Z. Breaking the symmetry of interfacial molecules with push-pull substituents enables 19.67% efficiency organic solar cells featuring enhanced charge extraction. *Energy Environ. Sci.* **2025**, *18*, 1722–1731.
- (3) Chen, Q.; Sun, K.; Franco, L. R.; Wu, J.; Ohlstrom, L.; Liu, X.; Gumbo, M.; Ozorio, M. S.; Araujo, C. M.; Zhang, G.; Johansson, A.; Moons, E.; Fahlman, M.; Yu, D.; Wang, Y.; Wang, E. Effects of Alkyl Spacer Length in Carbazole-Based Self-Assembled Monolayer Materials on Molecular Conformation and Organic Solar Cell Performance. *Adv. Sci.* **2025**, *12*, 2410277.
- (4) Liu, H.; Xin, Y.; Suo, Z.; Yang, L.; Zou, Y.; Cao, X.; Hu, Z.; Kan, B.; Wan, X.; Liu, Y.; Chen, Y. Dipole Moments Regulation of Biphosphonic Acid Molecules for Self-assembled Monolayers Boosts the Efficiency of Organic Solar Cells Exceeding 19.7%. *J. Am. Chem. Soc.* **2024**, *146*, 14287–14296.
- (5) Lin, Y.; Zhang, Y.; Zhang, J.; Marcinkas, M.; Malinauskas, T.; Magomedov, A.; Nugraha, M. I.; Kaltsas, D.; Naphade, D. R.; Harrison, G. T.; El-Labban, A.; Barlow, S.; De Wolf, S.; Wang, E.; McCulloch, I.; Tsetseris, L.; Getautis, V.; Marder, S. R.; Anthopoulos, T. D. 18.9% Efficient Organic Solar Cells Based on n-Doped Bulk-Heterojunction and Halogen-Substituted Self-Assembled Monolayers as Hole Extracting Interlayers. *Adv. Energy Mater.* **2022**, *12*, 2202503.
- (6) Lin, Y.; Firdaus, Y.; Isikgor, F. H.; Nugraha, M. I.; Yengel, E.; Harrison, G. T.; Hallani, R.; El-Labban, A.; Faber, H.; Ma, C.; Zheng, X.; Subbiah, A.; Howells, C. T.; Bakr, O. M.; McCulloch, I.; Wolf, S. D.; Tsetseris, L.; Anthopoulos, T. D. Self-Assembled Monolayer Enables Hole Transport Layer-Free Organic Solar Cells with 18% Efficiency and Improved Operational Stability. *ACS Energy Letters* **2020**, *5*, 2935–2944.
- (7) Zhang, B.; Zhao, Y.; Xu, C.; Feng, C.; Li, W.; Qin, X.; Lv, M.; Luo, X.; Qin, X.; Li, A.; He, Z.; Wang, E. Perylene Diimide-Based Low-Cost and Thickness-Tolerant Electron Transport Layer Enables Polymer Solar Cells Approaching 19% Efficiency. *Adv. Funct. Mater.* **2024**, *34*, 2400903.
- (8) Yu, Y.; Wang, J.; Cui, Y.; Chen, Z.; Zhang, T.; Xiao, Y.; Wang, W.; Wang, J.; Hao, X.-T.; Hou, J. Cost-Effective Cathode Interlayer Material for Scalable Organic Photovoltaic Cells. *J. Am. Chem. Soc.* **2024**, *146*, 8697–8705.
- (9) Jiang, H.; Liang, Q.; Guo, H.; Zhang, A.; Wang, X.; Tang, Z.; Bo, Z. All Roads Lead to Rome: Isomers with Divergent Cathode Modification Mechanisms toward Ohmic Contact. *J. Am. Chem. Soc.* **2024**, *146*, 30262–30271.
- (10) Wang, Z.; Ren, Y.; Meng, J.; Zou, X.; Wang, S.; Zhao, M.; Wang, H.; Hao, Y.; Xu, B.; Wang, E.; Yin, S. Realizing 18.03% efficiency and good junction characteristics in organic solar cells via hydrogen-bonding interaction between glucose and ZnO electron transport layers. *J. Mater. Chem. A* **2023**, *11*, 1810–1816.
- (11) Wu, J.; Sun, F.; Hua, F.; Hou, W.; Xia, X.; Guo, X.; Yu, D.; Wang, E.; Li, Y.; Zhang, M. Balance Processing and Molecular Packing via Structural Disorder in a Random Terpolymer for Over 19% Efficiency Non-Halogenated Solvent Organic Solar Cells. *Adv. Energy Mater.* **2025**, *15*, 250024.
- (12) Lin, C.; Chen, Z.; Peng, R.; Song, W.; Gao, J.; Yu, X.; Feng, T.; Bai, Y.; Ge, Z. Flexible spacer-block multi-component copolymerized donors enable resilient organic solar cells with over 40% crack-onset strain. *Energy Environ. Sci.* **2024**, *17*, 9359–9374.
- (13) Hao, S.; Xu, X.; Yu, L.; Peng, S.; Xia, J.; Xie, Y.; Duan, C.; Wu, H.; Li, R.; Peng, Q. Saddle-Shaped Third Component with Out-of-Plane Electrostatic Dipole for Realizing High-Performance Photovoltaic Donor Terpolymers. *Adv. Mater.* **2023**, *35*, 2301732.
- (14) Cheng, F.; Cui, Y.; Ding, F.; Chen, Z.; Xie, Q.; Xia, X.; Zhu, P.; Lu, X.; Zhu, H.; Liao, X.; Chen, Y. Terpolymerization and Regioisomerization Strategy to Construct Efficient Terpolymer Donors Enabling High-Performance Organic Solar Cells. *Adv. Mater.* **2023**, *35*, 2300820.
- (15) Ren, J.; Wang, J.; Qiao, J.; Chen, Z.; Hao, X.; Zhang, S.; Hou, J. Manipulating Aggregation Kinetics toward Efficient All-Printed Organic Solar Cells. *Adv. Mater.* **2025**, *37*, 2418353.
- (16) Li, C.; Song, J.; Lai, H.; Zhang, H.; Zhou, R.; Xu, J.; Huang, H.; Liu, L.; Gao, J.; Li, Y.; Jee, M. H.; Zheng, Z.; Liu, S.; Yan, J.; Chen, X.-K.; Tang, Z.; Zhang, C.; Woo, H. Y.; He, F.; Gao, F.; Yan, H.; Sun, Y. Non-fullerene acceptors with high crystallinity and photoluminescence quantum yield enable > 20% efficiency organic solar cells. *Nat. Mater.* **2025**, *24*, 433–443.
- (17) Lai, H.; Lang, Y.; Luo, Y.; Deng, Z.; Wang, Y.; Qiu, D.; Sun, R.; Zhang, G.; Wu, J.; Li, G.; He, F. Chlorine-Mediated Dispersion Modulates Packing Arrangement of Asymmetric Acceptors for High-Performance Organic Solar Cells. *Adv. Energy Mater.* **2025**, 2406097.
- (18) Chen, H.; Huang, Y.; Zhang, R.; Mou, H.; Ding, J.; Zhou, J.; Wang, Z.; Li, H.; Chen, W.; Zhu, J.; Cheng, Q.; Gu, H.; Wu, X.; Zhang, T.; Wang, Y.; Zhu, H.; Xie, Z.; Gao, F.; Li, Y.; Li, Y. Organic solar cells with 20.82% efficiency and high tolerance of active layer thickness through crystallization sequence manipulation. *Nat. Mater.* **2025**, *24*, 444–453.
- (19) Sun, Y.; Wang, L.; Guo, C.; Xiao, J.; Liu, C.; Chen, C.; Xia, W.; Gan, Z.; Cheng, J.; Zhou, J.; Chen, Z.; Zhou, J.; Liu, D.; Wang, T.; Li, W. π -Extended Nonfullerene Acceptor for Compressed Molecular Packing in Organic Solar Cells To Achieve over 20% Efficiency. *J. Am. Chem. Soc.* **2024**, *146*, 12011–12019.
- (20) Chen, S.; Zhu, S.; Hong, L.; Deng, W.; Zhang, Y.; Fu, Y.; Zhong, Z.; Dong, M.; Liu, C.; Lu, X.; Zhang, K.; Huang, F. Binary

Organic Solar Cells with over 19% Efficiency and Enhanced Morphology Stability Enabled by Asymmetric Acceptors. *Angew. Chem., Int. Ed.* **2024**, *63*, No. e202318756.

(21) Yang, X.; Sun, R.; Wang, Y.; Chen, M.; Xia, X.; Lu, X.; Lu, G.; Min, J. Ternary All-Polymer Solar Cells with Efficiency up to 18.14% Employing a Two-Step Sequential Deposition. *Adv. Mater.* **2023**, *35*, 2209350.

(22) Bai, Q.; Liang, Q.; Liu, Q.; Liu, B.; Guo, X.; Niu, L.; Sun, H. PY-IT, an Excellent Polymer Acceptor†. *Chin. J. Chem.* **2023**, *41*, 3714–3728.

(23) Chen, Z.; Li, X.; Qin, S.; Gong, Y.; Liu, Z.; Yuan, M.; Liang, T.; Meng, L.; Li, Y. Asymmetric Self-Assembled Monolayer as Hole Transport Layer Enables Binary Organic Solar Cells Based on PM6:Y6 with Over 19% Efficiency. *CCS Chem.* **2025**, *7*, S07–S18.

(24) Wang, Y.; Jiang, W.; Liu, S. C.; Lin, C. T.; Fan, B.; Li, Y.; Gao, H.; Liu, M.; Lin, F. R.; Jen, A. K. Y. Durable Organic Photovoltaics Enabled by a Morphology-Stabilizing Hole-Selective Self-Assembled Monolayer. *Adv. Energy Mater.* **2024**, *14*, 2303354.

(25) Yu, X.; Ding, P.; Yang, D.; Yan, P.; Wang, H.; Yang, S.; Wu, J.; Wang, Z.; Sun, H.; Chen, Z.; Xie, L.; Ge, Z. Self-Assembled Molecules with Asymmetric Backbone for Highly Stable Binary Organic Solar Cells with 19.7% Efficiency. *Angew. Chem., Int. Ed.* **2024**, *63*, No. e202401518.

(26) Li, M.; Liu, M.; Qi, F.; Lin, F. R.; Jen, A. K.-Y. Self-Assembled Monolayers for Interfacial Engineering in Solution-Processed Thin-Film Electronic Devices: Design, Fabrication, and Applications. *Chem. Rev.* **2024**, *124*, 2138–2204.

(27) Wang, W.; Lin, Z.; Gao, S.; Zhu, W.; Song, X.; Tang, W. Versatile Self-Assembled Hole Transport Monolayer Enables Facile Processing Organic Solar Cells over 18% Efficiency with Good Generality. *Adv. Funct. Mater.* **2023**, *33*, 2303653.

(28) Zhou, H.; Wang, W.; Duan, Y.; Sun, R.; Li, Y.; Xie, Z.; Xu, D.; Wu, M.; Wang, Y.; Li, H.; Fan, Q.; Peng, Y.; Yao, Y.; Liao, C.; Peng, Q.; Liu, S.; Liu, Z. Glycol Monomethyl Ether-Substituted Carbazolyl Hole-Transporting Material for Stable Inverted Perovskite Solar Cells with Efficiency of 25.52%. *Angew. Chem., Int. Ed.* **2024**, *63*, No. e202403068.

(29) Sun, X.; Zhang, C.; Yao, Y.; Lv, J.; Yao, J.; Ding, X.; Lu, M.; Zhu, L.; Zhang, G.; Lin, H.; Shi, Y.; Wang, K.; Yang, C.; Ouyang, X.; Hu, H.; McCulloch, I.; Lin, Y. 19.35% Efficient Binary Bulk-Heterojunction Organic Photovoltaic Enabled by Optimizing Bromine-Substituted Self-Assembled Carbazole Based Molecules. *Adv. Funct. Mater.* **2024**, *34*, 2406060.

(30) Li, M.; Li, Z.; Fu, H.; Yu, R.; Jiang, W.; Qi, F.; Lin, F. R.; Chen, G.; Walsh, A.; Jen, A. K.-Y. Molarly Engineered Self-Assembled Monolayers as Effective Hole-Selective Layers for Organic Solar Cells. *ACS Appl. Energy Mater.* **2024**, *7*, 1306–1312.

(31) Geng, R.; Gao, S.; Liu, J.; Zhou, X.; Sun, Z.; Ma, X.; Lu, X.; Xu, H.; Su, T.; Zhang, Z.; Chen, S.; Yin, J.; Song, X. Tuning interfacial interaction strategy by asymmetric configuration to construct self-assembly materials for efficient organic solar cells. *Chem. Eng. J.* **2024**, *483*, 149035.

(32) Lin, Y.; Magomedov, A.; Firdaus, Y.; Kaltsas, D.; El-Labban, A.; Faber, H.; Naphade, D. R.; Yengel, E.; Zheng, X.; Yarali, E.; Chaturvedi, N.; Loganathan, K.; Gkeka, D.; AlShammari, S. H.; Bakr, O. M.; Laquai, F.; Tsetseris, L.; Getautis, V.; Anthopoulos, T. D. 18.4% Organic Solar Cells Using a High Ionization Energy Self-Assembled Monolayer as Hole-Extraction Interlayer. *ChemSusChem* **2021**, *14*, 3569–3578.

(33) Geng, R.; Liu, P.; Pan, R.; Xu, H.; Gao, S.; Zhang, Z.; Su, T.; Wu, H.; Zhu, W.; Song, X. Self-assembled monolayers featuring multi-chlorinated carbazole unit for improving hole extraction efficiency in organic photoelectronic device. *Chem. Eng. J.* **2023**, *454*, 140138.

(34) Gao, S.; Peng, R.; Qiu, Y.; Liu, H.; Wu, Y.; Li, X.; Zhang, Y.; Jin, F.; Ge, Z. Conjugated Group Tuning of Self-Assembled Monolayer for Efficient Hole-Transport Layer in Organic Solar Cells. *Adv. Funct. Mater.* **2025**, *35*, 2418223.

(35) Levine, I.; Al-Ashouri, A.; Musiienko, A.; Hempel, H.; Magomedov, A.; Drevilkauskaitė, A.; Getautis, V.; Menzel, D.;

Hinrichs, K.; Unold, T.; Albrecht, S.; Dittrich, T. Charge transfer rates and electron trapping at buried interfaces of perovskite solar cells. *Joule* **2021**, *5*, 2915–2933.

(36) Vidyasagar, D.; Yun, Y.; Yu Cho, J.; Lee, H.; Won Kim, K.; Tae Kim, Y.; Woong Yang, S.; Jung, J.; Chang Choi, W.; Kim, S.; Kumar Gunasekaran, R.; Kang, S. B.; Heo, K.; Kim, D. H.; Heo, J.; Lee, S. Surface-functionalized hole-selective monolayer for high efficiency single-junction wide-bandgap and monolithic tandem perovskite solar cells. *J. Energy Chem.* **2024**, *88*, 317–326.

(37) Li, D.; Lian, Q.; Du, T.; Ma, R.; Liu, H.; Liang, Q.; Han, Y.; Mi, G.; Peng, O.; Zhang, G.; Peng, W.; Xu, B.; Lu, X.; Liu, K.; Yin, J.; Ren, Z.; Li, G.; Cheng, C. Co-adsorbed self-assembled monolayer enables high-performance perovskite and organic solar cells. *Nat. Commun.* **2024**, *15*, 7605.

(38) Park, S. M.; Wei, M.; Lempesis, N.; Yu, W.; Hossain, T.; Agosta, L.; Carnevali, V.; Atapattu, H. R.; Serles, P.; Eickemeyer, F. T.; Shin, H.; Vafaie, M.; Choi, D.; Darabi, K.; Jung, E. D.; Yang, Y.; Kim, D. B.; Zakeeruddin, S. M.; Chen, B.; Amassian, A.; Filleter, T.; Kanatzidis, M. G.; Graham, K. R.; Xiao, L.; Rothlisberger, U.; Gratzel, M.; Sargent, E. H. Low-loss contacts on textured substrates for inverted perovskite solar cells. *Nature* **2023**, *624*, 289–294.

(39) Mao, L.; Yang, T.; Zhang, H.; Shi, J.; Hu, Y.; Zeng, P.; Li, F.; Gong, J.; Fang, X.; Sun, Y.; Liu, X.; Du, J.; Han, A.; Zhang, L.; Liu, W.; Meng, F.; Cui, X.; Liu, Z.; Liu, M. Fully Textured, Production-Line Compatible Monolithic Perovskite/Silicon Tandem Solar Cells Approaching 29% Efficiency. *Adv. Mater.* **2022**, *34*, 2206193.

(40) Phung, N.; Verheijen, M.; Todinova, A.; Datta, K.; Verhage, M.; Al-Ashouri, A.; Kobler, H.; Li, X.; Abate, A.; Albrecht, S.; Creatore, M. Enhanced Self-Assembled Monolayer Surface Coverage by ALD NiO in p-i-n Perovskite Solar Cells. *ACS Appl. Mater. Interfaces* **2022**, *14*, 2166–2176.

(41) Zhang, A.; Li, M.; Dong, C.; Ye, W.; Zhu, Y.; Yang, J.; Hu, L.; Li, X.; Xu, L.; Zhou, Y.; Song, H.; Chen, C.; Tang, J. Role of NiO in wide-bandgap perovskite solar cells based on self-assembled monolayers. *Chem. Eng. J.* **2024**, *494*, 153253.

(42) Jiang, W.; Wang, D.; Shang, W.; Li, Y.; Zeng, J.; Zhu, P.; Zhang, B.; Mei, L.; Chen, X.-K.; Xu, Z.-X.; Lin, F. R.; Xu, B.; Jen, A. K.-Y. Spin-Coated and Vacuum-Processed Hole-Extracting Self-Assembled Multilayers with H-Aggregation for High-Performance Inverted Perovskite Solar Cells. *Angew. Chem., Int. Ed.* **2024**, *63*, No. e202411730.

(43) Zhang, S.; Ye, F.; Wang, X.; Chen, R.; Zhang, H.; Zhan, L.; Jiang, X.; Li, Y.; Ji, X.; Liu, S.; Yu, M.; Yu, F.; Zhang, Y.; Wu, R.; Liu, Z.; Ning, Z.; Neher, D.; Han, L.; Lin, Y.; Tian, H.; Chen, W.; Stolterfoht, M.; Zhang, L.; Zhu, W.-H.; Wu, Y. Minimizing buried interfacial defects for efficient inverted perovskite solar cells. *Science* **2023**, *380*, 404–409.

(44) Wang, W.; Wei, K.; Yang, L.; Deng, J.; Zhang, J.; Tang, W. Dynamic self-assembly of small molecules enables the spontaneous fabrication of hole conductors at perovskite/electrode interfaces for over 22% stable inverted perovskite solar cells. *Mater. Horiz.* **2023**, *10*, 2609–2617.

(45) Pitaro, M.; Alonso, J. S.; Di Mario, L.; Garcia Romero, D.; Tran, K.; Zaharia, T.; Johansson, M. B.; Johansson, E. M. J.; Loi, M. A. A carbazole-based self-assembled monolayer as the hole transport layer for efficient and stable Cs_{0.25}FA_{0.75}Sn_{0.5}Pb_{0.5}I₃ solar cells. *J. Mater. Chem. A* **2023**, *11*, 11755–11766.

(46) Fei, C.; Kuvayskaya, A.; Shi, X.; Wang, M.; Shi, Z.; Jiao, H.; Silverman, T. J.; Owen-Bellini, M.; Dong, Y.; Xian, Y.; et al. Strong-bonding hole-transport layers reduce ultraviolet degradation of perovskite solar cells. *Science* **2024**, *384*, 1126–1134.

(47) Lange, I.; Reiter, S.; Pätzelt, M.; Zykova, A.; Nefedov, A.; Hildebrandt, J.; Hecht, S.; Kowarik, S.; Wöll, C.; Heimel, G.; Neher, D. Tuning the Work Function of Polar Zinc Oxide Surfaces using Modified Phosphonic Acid Self-Assembled Monolayers. *Adv. Funct. Mater.* **2014**, *24*, 7014–7024.

(48) Wu, J.; Li, G.; Fang, J.; Guo, X.; Zhu, L.; Guo, B.; Wang, Y.; Zhang, G.; Arunagiri, L.; Liu, F.; Yan, H.; Zhang, M.; Li, Y. Random

terpolymer based on thiophene-thiazolothiazole unit enabling efficient non-fullerene organic solar cells. *Nat. Commun.* **2020**, *11*, 4612.

(49) Azzam, W.; Subaihi, A.; Rohwerder, M.; Bashir, A.; Terfort, A.; Zharnikov, M. Odd-even effects in aryl-substituted alkanethiolate SAMs: nonsymmetrical attachment of aryl unit and its impact on the SAM structure. *Phys. Chem. Chem. Phys.* **2024**, *26*, 7563–7572.

(50) Guan, S.; Li, Y.; Xu, C.; Yin, N.; Xu, C.; Wang, C.; Wang, M.; Xu, Y.; Chen, Q.; Wang, D.; Zuo, L.; Chen, H. Self-Assembled Interlayer Enables High-Performance Organic Photovoltaics with Power Conversion Efficiency Exceeding 20%. *Adv. Mater.* **2024**, *36*, 2400342.

(51) Bin, H.; Datta, K.; Wang, J.; van der Pol, T. P. A.; Li, J.; Wienk, M. M.; Janssen, R. A. J. Finetuning Hole-Extracting Monolayers for Efficient Organic Solar Cells. *ACS Appl. Mater. Interfaces* **2022**, *14*, 16497–16504.

(52) Li, M.; Li, Z.; Fu, H.; Yu, R.; Jiang, W.; Qi, F.; Lin, F. R.; Chen, G.; Walsh, A.; Jen, A. K. Y. Molecularly Engineered Self-Assembled Monolayers as Effective Hole-Selective Layers for Organic Solar Cells. *ACS Appl. Energy Mater.* **2024**, *7*, 1306–1312.

(53) Tu, S.; Chen, W.; Gang, Y.; Xiong, Q.; Li, X. Engineering a thermally robust hole-selective layer for stable flexible perovskite solar cells. *Chem. Eng. J.* **2025**, *503*, 158389.

(54) Liu, M.; Bi, L.; Jiang, W.; Zeng, Z.; Tsang, S.-W.; Lin, F. R.; Jen, A. K.-Y. Compact Hole-Selective Self-Assembled Monolayers Enabled by Disassembling Micelles in Solution for Efficient Perovskite Solar Cells. *Adv. Mater.* **2023**, *35*, 2304415.

(55) Huang, Y.; Tao, M.; Zhang, Y.; Wang, Z.; Sun, Z.; Zhang, W.; Xiong, Y.; Zong, X.; Wang, Y.; Liang, M. Asymmetric Modification of Carbazole Based Self-Assembled Monolayers by Hybrid Strategy for Inverted Perovskite Solar Cells. *Angew. Chem., Int. Ed.* **2025**, *64*, No. e202416188.

(56) Kim, D. H.; Lee, H. J.; Lee, S. H.; Kang, Y. J.; Kwon, S. N.; Kim, D. H.; Na, S. I. Mixed Self-Assembled Hole-Transport Monolayer Enables Simultaneous Improvement of Efficiency and Stability of Perovskite Solar Cells. *Sol. RRL* **2024**, *8*, 2400067.

(57) Singh, N.; Mohapatra, A.; Chu, C.-W.; Tao, Y.-T. Modulation of work function of ITO by self-assembled monolayer and its effect on device characteristics of inverted perovskite solar cells. *Org. Electron.* **2021**, *98*, 106297.

(58) Wang, S.; Chen, H.; Zhang, J.; Xu, G.; Chen, W.; Xue, R.; Zhang, M.; Li, Y.; Li, Y. Targeted Therapy for Interfacial Engineering Toward Stable and Efficient Perovskite Solar Cells. *Adv. Mater.* **2019**, *31*, No. e1903691.

(59) Lin, Y.; Zhang, Y.; Zhang, J.; Marcinskas, M.; Malinauskas, T.; Magomedov, A.; Nugraha, M. I.; Kaltsas, D.; Naphade, D. R.; Harrison, G. T.; et al. 18.9% Efficient Organic Solar Cells Based on n-Doped Bulk-Heterojunction and Halogen-Substituted Self-Assembled Monolayers as Hole Extracting Interlayers. *Adv. Energy Mater.* **2022**, *12*, 2202503.